Research Article | Vol. 14, No. 7 / 1 Jul 2024 / Optical Materials Express 1886
Optical Materials EXPRESS

Temperature dependence of THz generation efficiency, THz refractive index, and THz absorption in lithium-niobate around 275 GHz

UMIT DEMIRBAS,[1,2,3] CHRISTIAN RENTSCHLER,[1,4,5] ZHELIN ZHANG,[1,6] MIKHAIL PERGAMENT,[1] NICHOLAS H. MATLIS,[1] AND FRANZ X. KÄRTNER[1,4,7,*]

[1]*Center for Free-Electron Laser Science CFEL, Deutsches Elektronen-Synchrotron DESY, Notkestr. 85, 22607 Hamburg, Germany*
[2]*Paul Scherrer Institut, CH-5232 Villigen PSI, Switzerland*
[3]*Antalya Bilim University, 07190 Dosemealti, Antalya, Turkey*
[4]*Physics Department, University of Hamburg, Luruper Chaussee 149, 22761 Hamburg, Germany*
[5]*Max Planck School of Photonics, Hans-Knöll-Straße 1, 07745 Jena, Germany*
[6]*Tsung-Dao Lee Institute, Shanghai Jiao Tong University, Shanghai 200240, China*
[7]*The Hamburg Centre for Ultrafast Imaging, Luruper Chaussee 149, 22761 Hamburg, Germany*
[*]*franz.kaertner@desy.de*

Abstract: In this study, we demonstrate the capabilities of the pulse train excitation approach in determining key material properties of nonlinear crystals, such as refractive index, thermo-optic coefficient, and absorption. The method provides reliable results even at relatively low THz frequencies, where other characterization methods, such as THz time-domain spectroscopy, have difficulties. To illustrate the capabilities of our approach, we used pulse trains with 800-fs long pulses and adjustable time delay to investigate the material properties of periodically poled lithium niobate (PPLN) crystal with a poling period of 400 µm. Via scanning the incident pulse-train frequency, we measured the frequency response of the crystal at different temperatures (78-350 K), which enabled us to determine the temperature dependence of the refractive index and thermo-optic coefficient of the PPLN crystal around 275 GHz with very high precision. We further studied the variation of THz generation efficiency with temperature in detail to understand the temperature dependence of THz absorption in PPLN material. The technique employed is quite general and could be applied to both other frequency ranges and nonlinear crystals.

1. Introduction

High-energy and high-field table-top THz sources are attractive for many applications, including spectroscopy, microscopy, imaging, metrology, communications, and medical diagnostics/treatment [1–3]. Optical rectification (OR) of ultrashort laser pulses is a well-established technique to generate (i) single-cycle THz pulses with broad spectra and high peak field or (ii) narrow-band and multicycle (MC) THz pulses with ample spectral brightness [4]. So far, most of the work with ultrashort laser-based THz sources has focused on generating single-cycle THz pulses [5–9] due to their high electric field strength and broad bandwidth. However, over the last few years, there has been a growing interest in the development of MC THz pulses as well [10–18] for applications such as particle acceleration [10], spectroscopy [19,20], and coherent control of matter [21] where resonant excitation via tunable narrowband sources has advantages over broadband excitation.

#528491 https://doi.org/10.1364/OME.528491
Journal © 2024 Received 29 Apr 2024; revised 16 Jun 2024; accepted 17 Jun 2024; published 27 Jun 2024

Optical Materials EXPRESS

A well-known method for generating narrowband multi-cycle THz sources is to exploit the velocity mismatch between the optical and THz pulses in poled nonlinear crystals such as PPLN [4]. Via quasi-phase-matching (QPM) in these structures, a THz waveform that corresponds to the domain structure of the poled nonlinear crystal is obtained [22]. MC THz pulses could also be obtained via spatial, temporal, and/or spectral shaping of the pump pulses using phase masks [23], transient gratings [24], spatial light modulators [25], chirped pulse-beating [14], two-line seeding [11], and Michelson interferometer-based pulse dividers [26]. If one combines these pump pulse shaping techniques with periodically poled crystals (such as PPLN), then both the pump source and the periodically poled crystal structure contribute to the narrowing of the multi-cycle THz wave.

In our recent work [26], we have used a train of sub-ps optical pulses (generated via a Michelson interferometer-based pulse divider setup) to excite PPLN in cryogenic operation and shown that this system (i) enables precise parameter control of the generated MC THz pulse, (ii) allows mapping of the key properties of the nonlinear medium used with unprecedented precision, and (iii) empowers generation of THz spectra with record spectral brightness levels. In [26], we have also provided a detailed analytical model that can be used to understand the role of periodically-poled crystals and the pulse train in the MC THz generation process.

In this follow-up study, we demonstrate frequency mapping characteristics of the pulse train in more detail by measuring the temperature dependence of important optical properties of PPLN, such as refractive index, thermo-optic coefficient, and absorption coefficient around a central THz frequency of 275 GHz. This is the frequency range where other material characterization methods, such as THz time-domain spectroscopy, have difficulties providing the required precision [27–30].

2. Experimental setup

A home-built laser system consisting of a seeder, a regenerative amplifier (regen), and a multi-pass amplifier was developed as the pump source for THz generation. This system has been recently introduced in detail in [26], so here our discussion will be brief (see Fig. 1(a) in [26] for further details). The Yb-fiber-based seeder system provides 10 nJ pulses at 40 MHz at a central wavelength of 1034 nm and a bandwidth of 10 nm. The seder is followed by a pulse divider setup (see Fig. 1(b) in [26]), which consists of eight polarization-based Michelson interferometers (pulse divider stages), and enables the generation of a pulse train with an adjustable pulse number (from 1 to 2^8 : 256). The distance between the pulses could be freely adjusted by controlling the length of the interferometer arms.The nJ pulse energies of the pulse train (pulse burst) are first amplified in a room-temperature Yb:KYW regenerative amplifier up to 2.5 mJ energy [31]. The regen output is then further scaled up to 25 mJ in a room-temperature 4-pass Yb:YAG amplifier. Due to further gain narrowing in the Yb:YAG crystal, the final spectral width of the pulses is reduced to 1.9 nm. The pulses could be compressed down to 800 fs (estimated time-bandwidth product is around ~0.4, assuming a $Sech^2$ pulse shape). Due to thermal effects, the amplifier is operated at 10 Hz, but a future design based on a cryogenic Yb:YLF amplifier [32,33] operating at 1 kHz will be in operation in the coming years to reduce data-taking times in future studies.

For THz generation experiments, the compressed pulse train is sent into a commercial (HC Photonics Corp.) PPLN crystal with a poling period of 400 μm (Fig. 1). The PPLN crystal had an aperture of 4×4 mm^2 and a length of 20 mm (the 4 mm thickness is currently the largest thickness that could be commercially obtained). For the 20 mm length, the crystal contains (20/0.4) 50 poling periods (N_{PPLN} as defined in [26]). The lithium niobate sample used in this study was grown from a congruently melted composition and doped with 5% magnesium oxide (MgO) to minimize green-induced infrared absorption and photorefractive beam distortions (in literature these crystals are named as MCLN, C indicating the congruent growth, and M indicating MgO doping). The crystal was placed inside a dewar and cooled to cryogenic temperature.

Optical Materials EXPRESS

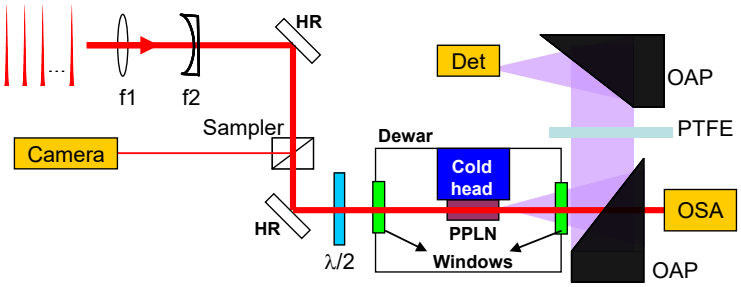

Fig. 1. Schematic layout of the THz generation setup used in the experiments. OAP: Off-axis parabola, OSA: Optical spectrometer, Det: THz energy meter, HR: Pump high-reflector.

Using a telescope consisting of lenses with focal lengths of 10 cm and −5 cm (f1 and f2 in Fig. 1), the $1/e^2$ diameter of the pump beam on the crystal is adjusted to a beam size of 3 mm on the crystal. The 4×4 mm^2 aperture of the PPLN crystal enabled a throughput of around 97% through the crystal aperture for this beam size. Note that using smaller beam sizes reduces THz efficiencies due to undesired effects such as self-focusing in LN (a topic that will be discussed in detail in a follow-up study) [34]. Hence, the pump beam diameter on the PPLN is kept at 3 mm despite the minor aperture effects. The THz radiation is generated collinearly with the laser beam and collected and focused onto a THz detector (Gentec SDX-1152 with a 9 mm diameter active area) by a pair of 10 cm focal length, 2-inch off-axis parabolas (OAPs) with a protected gold coating. The pump beam and the THz radiation polarization are parallel to the extraordinary axis of the lithium niobate crystal (all polarized along the z-axis to benefit from the large d_{33} coefficient of LN). The output of the Gentec detector is monitored with an oscilloscope. The voltage reading in the scope is converted into a THz energy with a conversion factor of (74 ± 3) mV/μJ (calibration of the detector is performed in-house by comparing its reading with a calibrated sensor from Lasertechnik GmbH) [6,35]. A 1 cm thick Teflon slab was inserted between the two OAP mirrors to entirely block the remaining pump beam (the filter had a transmission of 83% around 300 GHz [26]). The first OAP mirror had a 3 mm wide through-hole to allow passage of most of the pump beam (MPD249H-M01), which is then used to characterize the changes in the spectral content of the transmitted pump beam. The second OAP mirror also contained a through-hole to allow passage of a portion of the compressed seed beam for electro-optic sampling of the THz field (not shown in Fig. 1). For the EO sampling experiments, a 0.5 mm thick 10×10 mm^2 aperture <110> cut ZnTe crystal is employed.

3. Results and discussions

3.1. *Temperature dependence of frequency response of PPLN and estimation of THz refractive index and thermo-optic coefficient*

After confirming the calibration of the pulse train frequency scan system very carefully (see Appendix for details), we have measured the frequency response of the PPLN crystal using the pulse train as a function of temperature for temperatures between 78 K and 350 K. Figure 2 provides measured frequency response curves (tuning curves) at selected temperatures. As we can see from Fig. 2, the peak response of the crystal shifts from around 286.5 GHz at 78 K to 253 GHz at 350 K. The measured shift is mostly due to the change in the phase refractive index of the THz wave with temperature. We repeated this experiment three times on different days, and the measured data confirmed each other quite well (Data 1 to 3 in Fig. 3).

The following simple analytic formula could be used to model the measured temperature dependence of the resonance THz frequency (f_{THz}) for the 400 μm QPM MCLN crystal used in

Optical Materials EXPRESS

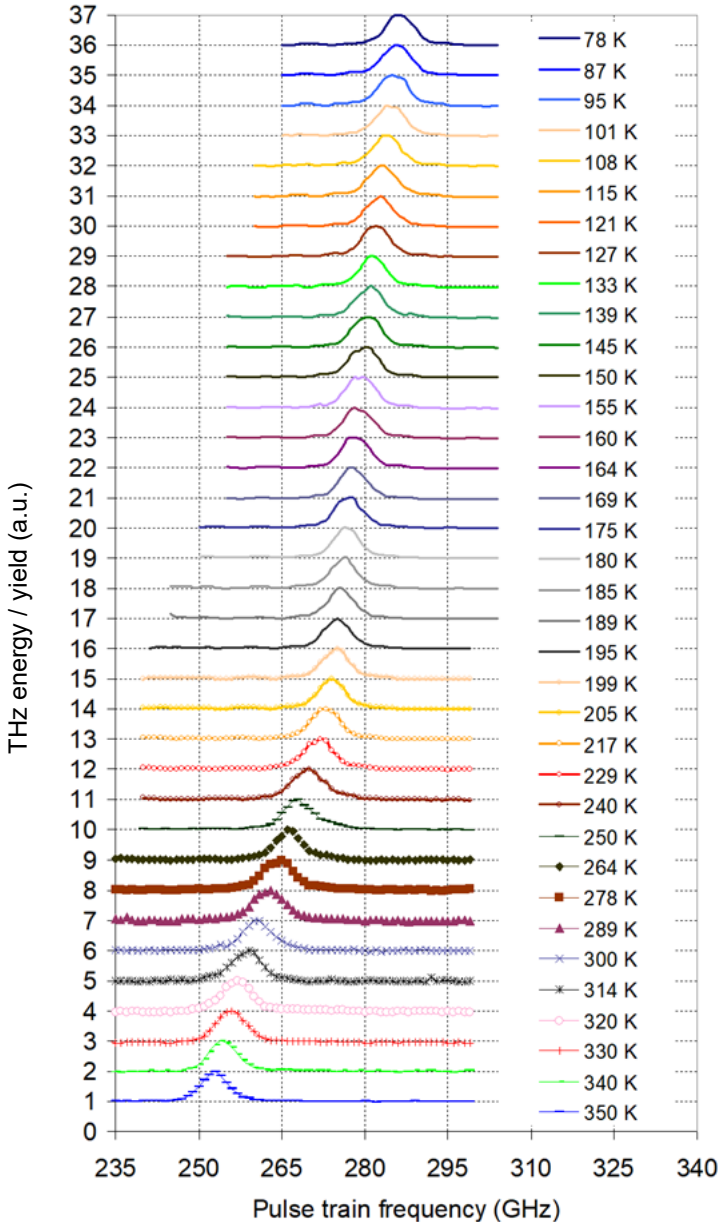

Fig. 2. Measured frequency response (tuning curves) of the PPLN crystal as a function of temperature between 78 K and 350 K. The data is taken with the 2 cm long PPLN crystal with a QPM period of 400 μm at an incident energy of 4 mJ, a pump diameter of 3 mm, and a pulse burst of 64 pulses.

Optical Materials EXPRESS

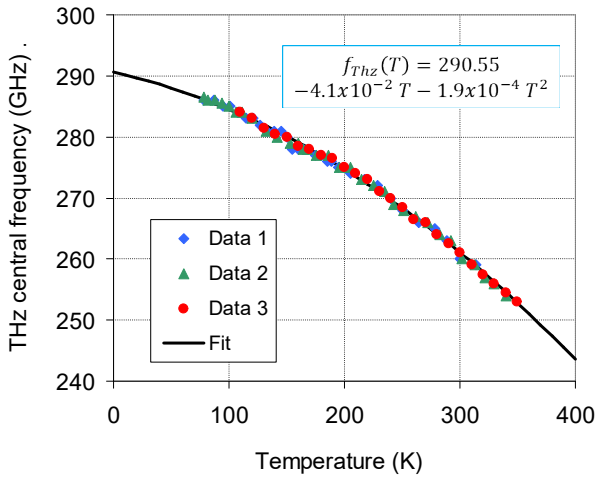

Fig. 3. Measured variation of THz central frequency as a function of PPLN crystal temperature. The solid curve is an analytical fit to the measured data. A 5% MgO-doped congruently grown lithium niobate (MCLN) with a QPM period of 400 μm was used in the experiments.

this study:

$$f_{THz}(T) = 290.55 - 4.1 \cdot 10^{-2}\,T - 1.9 \cdot 10^{-4}\,T^2 \tag{1}$$

In Eq. (1), f_{THz} has the units of GHz, and T is the temperature in the units of Kelvin. Note that we have used step sizes of 0.25-0.5 GHz in our measurements; hence, the error bar due to the frequency resolution limit we have chosen is around ±0.1-0.2%.

There is little detailed report on temperature tuning of the THz frequency for PPLN in the literature to directly compare our data. In general, the measured trend in this study is quite similar to earlier reported frequency tuning curves at higher (>1 THz) frequencies [36]. As a side note, as one increases the temperature due to increased absorption losses of the PPLN crystal, the obtainable THz energies decrease significantly, which is also observed during these frequency scans, but in Fig. 2, we have chosen to show the curves on a normalized scale, as we want to focus on variation of resonance frequency peaks with temperature. For completeness, we show sample frequency scan curves taken at selected temperatures in Fig. 4, where we normalized all the curves to the maximum energy level obtained at 78 K. The variation of THz efficiency/yield with temperature will be discussed in detail in the next section.

The measured variation of the THz resonance frequency with temperature could then be used to calculate the refractive index of the THz wave in PPLN as a function of temperature (for the extraordinary axis). It is well-known that, for the forward propagating THz wave, the phase matching condition supports a THz wave with a central frequency (f_{THz}) of [4]:

$$f_{THz} = \frac{c}{\Lambda(\Delta n)} = \frac{c}{\Lambda(n_{THz} - n_{gr}^{opt})} \tag{2}$$

Here, c is the speed of light, Λ is the QPM orientation reversal period (400 μm in our case), n_{gr}^{opt} is the optical group velocity refractive index, and n_{THz} is the phase refractive index for the THz wave, and Δn is the difference between the THz-phase and optical group indices. Measured data in Fig. 3 and Eq. (2) could then be used to estimate the temperature dependence of the refractive index of the THz wave around the central frequency of 275 GHz. Here, we ignore variation of THz refractive index with frequency in the 253-286.5 GHz range, and the estimated error bar due to this simplification is around ±0.01%, much below our experimental error bars [37].

Optical Materials EXPRESS

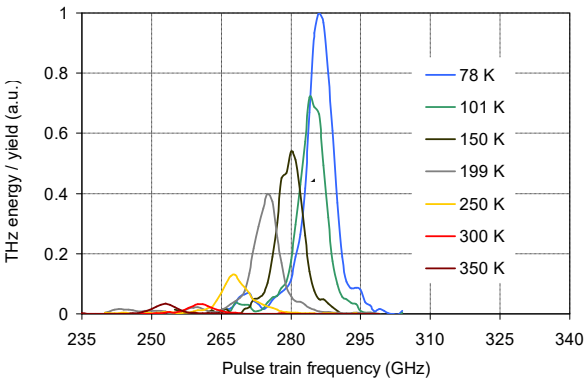

Fig. 4. Measured frequency scan curves of PPLN at selected temperature between 78 K and 350 K. The data is normalized to the maximum energy obtained at 78 K and clearly shows the effect of absorption in reducing THz yield. The data is taken with the 2 cm long PPLN crystal with a QPM period of 400 μm at an incident energy of 4 mJ, a pump diameter of 3 mm, and a pulse burst of 64 pulses.

While calculating the THz refractive index using Eq. (2), one should consider the temperature dependence of lithium niobate's optical group velocity refractive index [38,39]. Here, the growth condition (congruent or stoichiometric) and the MgO doping level of the sample cause slight changes in the reported refractive index values [38–41]. Unfortunately, to our knowledge, the temperature dependence of the refractive index for the pump wavelength has not been studied at cryogenic temperatures yet for LN, and the reported data is for room and elevated temperatures [38–40] . Here, after carefully investigating the reported data in the literature, we have chosen to use the Sellmeier equations provided by Paul et al. in [38] for 5% MgO-doped congruent LN (the slope of variation of group velocity refractive index with temperature is similar to what is reported by Jundt et al. [40] and Edwards et al. [39] for CLN). Using the formula given in [38], we have calculated the group refractive index of 5% MgO CLN in its extraordinary axis as 2.209 at 300 K and as 2.191 at 78 K for a central wavelength of 1030 nm (only a 0.8% decrease with temperature is estimated due to the small thermo-optic coefficient of LN for the near-infrared wavelengths).

While using Eq. (2), one needs to also consider the variation of the QPM period with temperature due to thermal expansion, and for that, we have used the linear thermal expansion data given in [42]. Here, one can calculate that the QPM period, which is 400 μm at room temperature, shrinks to 399.77 μm at 78 K. The estimated reduction in QPM period length is only 0.06%. One thing to note is that here, we assume that (i) the value for the QPM period given by the manufacturer is correct and (ii) the variation of the QPM period over the crystal length is also minor.

Figure 5 summarizes the calculated results for Δn and THz refractive index (n_{THz}) for the extraordinary axis of 5% MgO-doped CLN. For comparison with the literature, we have also included the reported values of the THz refractive index for MCLN for different MgO doping levels [30,37] in Fig. 5. One thing to notice is that the pulse-train approach has enabled us to acquire much denser data points compared to most of the earlier reports, which only present results in a few selected temperatures (as the data taking and analysis time is much longer in alternative methods). To our knowledge, the literature lacks MCLN data for 5% MgO doping, but our results are in between what is reported by Pálfalvi et al. [37] and Wu et al. [30] for ~6% MgO-doped CLN samples (there is up to around ±2% difference between our results and the

Optical Materials EXPRESS

reports of Pálfalvi et al. and Wu et al. [30,37]). We estimate a THz refractive index of 4.81 at 78 K and 5.09 at 300 K for a central frequency of around 300 GHz.

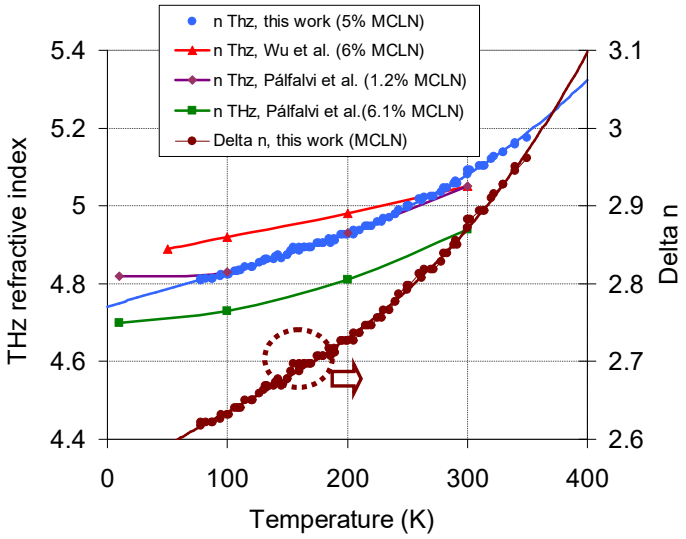

Fig. 5. Calculated variation of the phase refractive index of the THz wave with temperature at frequencies around 275 GHz for the extraordinary axis of lithium niobate. The solid curve is an analytical fit to the measured data (Eq. (3)). Comparison with the data in the literature [30,37] is also given. For the sake of completeness, we also plot Δn (the difference between THz phase refractive index and optical group index for the extraordinary axis of lithium niobate). The experiments used 5% MgO-doped congruently grown lithium niobate (MCLN).

The most significant error bar in our estimation for THz refractive index calculations is potentially coming from the Sellmeier equations used for the optical group refractive index, and hence, we also report Δn in Fig. 5. We estimate a Δn of 2.62 at 78 K and 2.88 at 300 K for a central frequency of around 275 GHz. For comparison, for higher THz frequencies (~1-2 THz) and for a pump wavelength of around 0.8 μm, Lee et al. reported a Δn of ~2.72 and ~2.91 at 78 and 300 K, respectively, for a PPLN sample [36]. Here, the pump wavelength, the THz frequencies, and the MgO doping of the samples are different, which might be causing the reported difference.

We provide the following analytical equations that could be used to estimate the temperature variation of THz refractive index and Δn around a center frequency of 275 GHz:

$$n_{THz}(T) = 4.74 + 1 \cdot 10^{-3}\ T - 1.65 \cdot 10^{-6}\ T^2 + 7 \cdot 10^{-9}\ T^3 \tag{3}$$

$$\Delta n(T) = 2.545 + 1 \cdot 10^{-3}\ T - 1.73 \cdot 10^{-6}\ T^2 + 6.7 \cdot 10^{-9}\ T^3 \tag{4}$$

In Eqs. (3,4) temperature T has the units of Kelvin. Note that, as our temperature-dependent THz data is taken with a large data set, it can also be used to calculate the thermo-optic coefficient (dn/dT) quite accurately (basically via just taking a derivative of Eq. (3)):

$$\frac{dn_{THz}}{dT}(T) = 1 \cdot 10^{-3}\ - 3.3 \cdot 10^{-6}\ \mathrm{T} + 2.1 \cdot 10^{-8}\ T^2. \tag{5}$$

In Eq. (5), dn/dT is in units of 1/K, and T again has the units of Kelvin. Using Eq. (5) we estimate the thermo-optic coefficient for LN near 275 GHz as 0.00087/K and 0.0019/K at 78 K and 300 K, respectively. Our value at room temperature (0.0019/K) is rather close to what has

Optical Materials EXPRESS

been reported by Sowade et al. (0.0013/K) for a center frequency of 1.4 THz [43]. As the frequency of Sowade et al. is close to the resonance peak of LN around 7.4 THz [13], it is reasonable that our estimate for the thermo-optic coefficient around 300 GHz is smaller than what is reported for 1.4 THz [43].

3.2. Temperature dependence of THz efficiency and absorption coefficient in PPLN

Once the central frequency of operation at different temperatures is determined, as the next step, we took THz generation efficiency curves at different temperatures. Figure 6 shows sample THz efficiency data taken at selected temperatures between 78 and 350 K. For each temperature, the pulse train frequency is adjusted to match the resonance frequency of the PPLN crystal at hand at that temperature (indicated in data captions). We see from Fig. 6 that, as expected, the THz efficiency increases with decreasing temperature mainly due to the reduction of PPLN material absorption. We have achieved the best performance at 78 K (around 286 GHz), producing an internal THz energy of around 25 μJ at a pump energy of 5.4 mJ. For the 3 mm beam, this corresponds to an internal efficiency of 0.45% at a peak fluence of 150 mJ/cm^2. Note that the efficiency achieved here is well above the Manley-Rowe limit (0.09%) due to the cascading process [4], which shows that, on average, each pump photon generates 5 THz photons. A fair parameter to compare the results obtained in different studies is efficiency per fluence. The 0.45% efficiency obtained around 286 GHz at the peak fluence of 150 mJ/cm^2 then corresponds to a value of 3 x10^{-3}%/(mJ/cm^2), very similar to what we have recently obtained (2.5×10^{-3}%/(mJ/cm^2)) around 347 GHz [26]. At room-temperature operation, at the same fluence level of 150 mJ/cm^2, the THz energy was as low as 0.7 μJ, corresponding to an internal efficiency of around 0.014%. This corresponds to more than 30 times lower energy at 300 K compared to 78 K: basically, for this 2 cm long crystal, the THz absorption limits the performance quite dramatically at room temperature (room-temperature performance will be better using a short crystal).

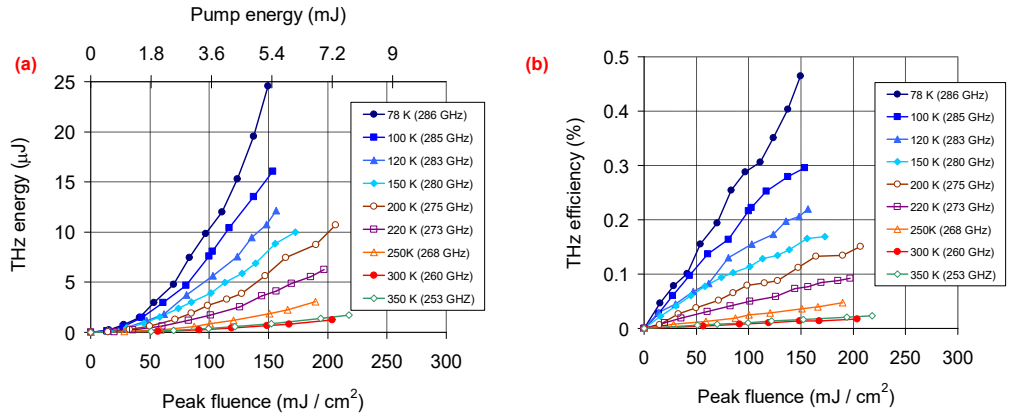

Fig. 6. Measured variation of (a) internal THz energy and (b) internal THz efficiency curves at selected temperatures between 78 K and 350 K. The data is taken using a 3 mm diameter pump beam size and using a pulse train consisting of 64 pulses.

We can then look at the variation of THz generation efficiency with temperature at fixed fluence values in more detail to try to understand the variation of THz absorption with temperature. For that, Fig. 7 shows the measured variation of THz efficiency with temperature at selected peak fluence values between 100-160 mJ/cm^2. Note that the measurement was repeated four times on different days. Some of the data is taken from the frequency scan experiments summarized in the earlier section (e.g., Fig. 4), and the remaining are taken from the data presented in Fig. 6. All the data is normalized to the maximum THz energy measured at 78 K. Undoubtedly, there are

Optical Materials EXPRESS

some fluctuations in the data, and the data sets taken in different days differ from each other (up to 10-20% around 150-200 K). On the other hand, one can still use the general trend in the data for some basic observations. From Fig. 7, we see that, first, when the temperature of the PPLN crystal is increased from 78 K to 120 K, the THz efficiency drops sharply. Then, between 120 K and ~175 K, we have a plateau-like region where the THz efficiency only decreases slightly with temperature. Later, between 200 K and 300 K, we observe another relatively substantial decrease in efficiency (but indeed not as sharp as the 78-120 K range). Finally, above 300 K, the efficiency is almost constant, and it even increases slightly with temperature (we have repeatedly measured a slightly higher efficiency at 350 K compared to 300 K).

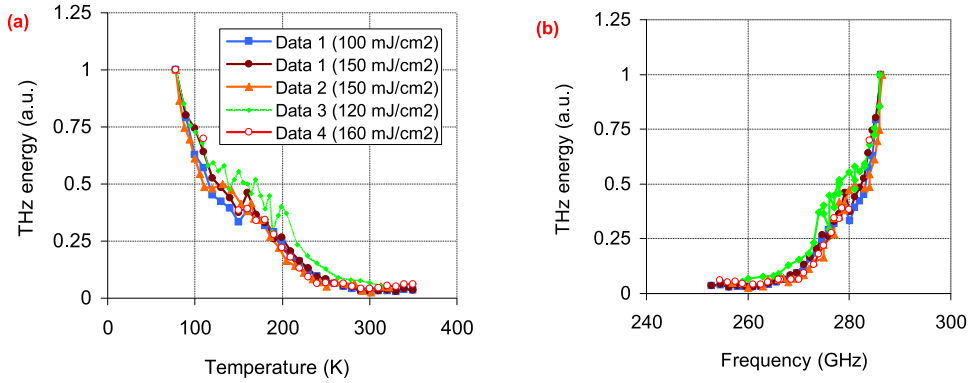

Fig. 7. (a) Measured variation of normalized THz energy with temperature at several different levels of pump peak fluence. (b) Variation of normalized THz energy with THz central frequency upon temperature tuning.

Several groups have reported the variation of THz efficiency with temperature in lithium niobate earlier [7,8,15,16,44,45], and there is quite a significant difference in reported data. The variation of THz generation efficiency with temperature is dependent on many factors, such as the frequency of the THz generated, the method used for THz generation, the pump pulse shape, and the length of the crystal used for THz generation. Hence, a considerable difference between reported data is expected. In general, the trend observed in our work is closest to what is reported in [45] around 1.7 THz using a 7.2 mm length crystal with a QPM period of 60 μm.

The main trend of decrease in THz efficiency with increasing temperature could be explained mainly by the increase of absorption in the PPLN crystal. On top of this, it is relatively well-known that the effective nonlinear optical coefficient, which is proportional to the electro-optic coefficient at these frequencies, is also temperature-dependent [13,27,46] and its value is measured to increase with temperature [47,48] due to the increase of the contribution coming from the ionic nonlinear influence [13]. The experimental results provided by Herzog et al. [47] could be used to model the temperature dependence of the effective nonlinear optical coefficient (d_{33}):

$$d_{eff}(T) = d_{eff\ @\ 295\ K}\ (0.79\ + 2.44 \cdot 10^{-6}\ T^2). \tag{6}$$

In Eq. (6), T is the temperature in Kelvin units and $d_{eff\ @295K}$ is the effective nonlinear optical coefficient of lithium niobate at room temperature.

To understand the other factors influencing the efficiency via temperature change, one needs to look at the basic analytical formula for estimating THz efficiency. Assuming plane waves and a nondepleted pump, the efficiency of THz generation via optical rectification using a bandwidth-limited ultrashort pulse can be estimated using [4]:

$$\eta_{THz} = g_{bw} \frac{\Omega_0^2\ d_{eff}^2\ L_{eff}}{\varepsilon_0 c^2 n_{THz}\ n_{pump}^2\ \Delta n} F_{pump}. \tag{7}$$

Optical Materials EXPRESS

In Eq. (7), ε_0 is the permittivity of free space, c is the speed of light, n_{pump} is the optical refractive index at the pump wavelength, Ω_0 is the central angular frequency of THz at the corresponding resonance, F_{pump} is the pump fluence, and L_{eff} is the effective crystal length. The effective crystal length is reduced due to the absorption, and we have used the following model for an estimation:

$$L_{eff} = \frac{1 - e^{-2\alpha L}}{2\alpha}. \tag{8}$$

Note that in Eq. (8), L is the crystal length, and α is the THz absorption coefficient (for our case, in the extra-ordinary axis and around a central frequency of 275 GHz). For small absorption values, L_{eff} is equal to the crystal length (L), and for large absorption values, it can be approximated by $\sim 1/\alpha$.

From Eqs. (7,8), we see that besides absorption and the nonlinear optical coefficient, the temperature dependence of the central frequency of THz (Ω_o, or $2\pi f_o$), the THz refractive index (n_{THz}), and the difference between the THz and optical group refractive index (Δn) also influence the THz efficiency. To understand the role of each in our case, in Fig. 8(a), we show the measured overall efficiency as a function of temperature (red solid curve is an exponential best fit to the measured data, which is shown by red open markers), along with calculated contributions of different factors. We observe that, with increasing temperature, the effective nonlinearity is expected to increase the THz efficiency, and the remaining factors all tend to decrease it. As a simple first-order analysis, using Eq. (7) and known/measured variation of n_{THz}, Ω_o, Δn, d_{eff} and n_{pump}, we have tried to isolate the effect of absorption, and the green solid line in Fig. 8(a) shows the estimated impact of absorption on reducing L_{eff} with increasing temperature. Interestingly, for the case studied, all the other factors almost balance out, and the estimated variation of L_{eff} with the temperature almost follows the measured overall efficiency trend (the red and green solid curves almost overlap with each other).

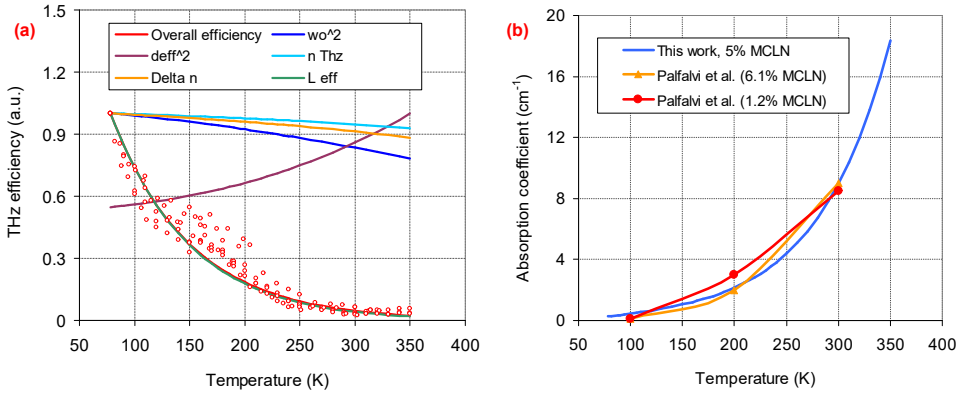

Fig. 8. (a) Measured variation of THz efficiency with PPLN crystal temperature is shown along with the calculated influence of other factors on efficiency such as THz refractive index ($1/n_{THz}$), the square of THz frequency (f^2), the square of the effective nonlinear optical coefficient (d_{eff}^2), and effective crystal length (L_{eff}). (b) Calculated variation of the temperature dependence of the absorption coefficient in lithium niobate near 275 GHz and comparison of the data with the literature [37]. For the Palfalvi et al. results presented in Fig. 8(b), we used a 2nd order interpolation to estimate the absorption near 275 GHz, as the data in [37] do not extend to these low frequencies.

As the second step, using the estimated variation of effective crystal length with temperature, we have tried to estimate the absorption of the LN crystal by using Eq. (8). For that, as a calibration point to our estimation, we have taken the absorption coefficient at room temperature

Optical Materials EXPRESS

as 9 cm^{-1} [37]. Our absorption coefficient estimate results are shown in Fig. 8(b). For 5% MCLN, we estimate a THz absorption of around 0.26 cm^{-1} at 78 K, 0.45 cm^{-1} at 100 K, 1.06 cm^{-1} at 150 K, 2.15 cm^{-1} at 200 K, 4.4 cm^{-1} at 250 K and 18.4 cm^{-1} at 350 K for a central frequency of around 275 GHz (assuming an absorption coefficient of 9 cm^{-1} at 300 K [37]). We see that the overall shape of absorption versus temperature is in relatively good agreement with the earlier results presented by Palfavi et al. [37].

We estimate the absorption coefficient here by making a rough exponential fit to the efficiency data in Fig. 8(a). Alternative polynomial fits to the same data will result in different absorption estimation curves. Moreover, the method employed for an absorption estimate based on efficiency data has relatively large error bars, as efficiency depends on many factors besides absorption, as we discussed earlier. As an alternative method, the measured tuning curves (frequency scans shown in Fig. 2), could also be used to estimate the absorption coefficient, as the width of the measured tuning curve is broadened with absorption (see Eq. (2) in [26]). However, as it is discussed in detail [26] as well (see Fig. 3 in [26]), for very small absorption values (below 1 cm^{-1}), the change in the width of the tuning curve is rather small, reducing the method's sensitivity. Despite all these issues, there is little THz absorption data for PPLN in the literature, especially at these low frequencies, and the absorption data presented here enables an initial insight into this.

4. Conclusions

In this work, using a flexible pulse train with adjustable frequency as an excitation source as well as a probing tool [26], we have measured the temperature dependence of frequency response of PPLN crystal near 275 GHz. The method enabled fast and precise determination of the THz refractive index and thermo-optic coefficient in the extraordinary axis of lithium niobate. We have also used the measured variation of THz generation efficiency with temperature to study the temperature dependence of the absorption coefficient of lithium niobate, but here, accurate estimation is more challenging since the THz efficiency depends on many other factors. We believe that the pulse train excitation/ probing approach could become a useful alternative tool for mapping the material properties of nonlinear crystals, especially at low frequencies where other methods, such as THz time-domain spectrometry, have intrinsic difficulty in providing reliable results.

Appendix

5.1 Calibration of pulse train frequency and confirmation with EO sampling

For the proposed method to work accurately, the correct frequency mapping capability of the pulse train needs to be confirmed [26]. This is required as the accurate mapping capability of the pulse train depends on the correct adjustment of distances in the pulse train divider setup interferometer arms. For high-precision adjustment of the lengths of the interferometer arms (with sub-10 μm precision), we have investigated several methods such as spectral interference, spatial interference, autocorrelation, and THz efficiency scan. Among the methods used, we have seen that autocorrelation is the most straightforward approach while adjusting the distances of the first five stages.

For example, Fig. 9(a) shows the recorded autocorrelation of the pulse train for a central frequency of 500 GHz. In this example, we see the pulses from the first five divider stages, where the pulse burst has 32 pulses, and the autocorrelation trace shows 63 peaks. The distance between the peaks is 2 ps, as shown in Fig. 9(b). The resolution of this method in the time domain is limited by the pulse width of the pulses in the pulse bunch. For this test, we readjusted the pre-compressor to compress the seeder pulses to around 300 fs, which provided us with a pulse timing adjustment error of about ±10 fs, which corresponds to a distance adjustment

Optical Materials EXPRESS

error of around ±3 µm. It is essential to state that one needs to confirm the calibration of the autocorrelator for this method to work correctly, as our device was initially measuring the pulses 5.4% shorter, and we have recalibrated our autocorrelator for the proper setting of the distances.

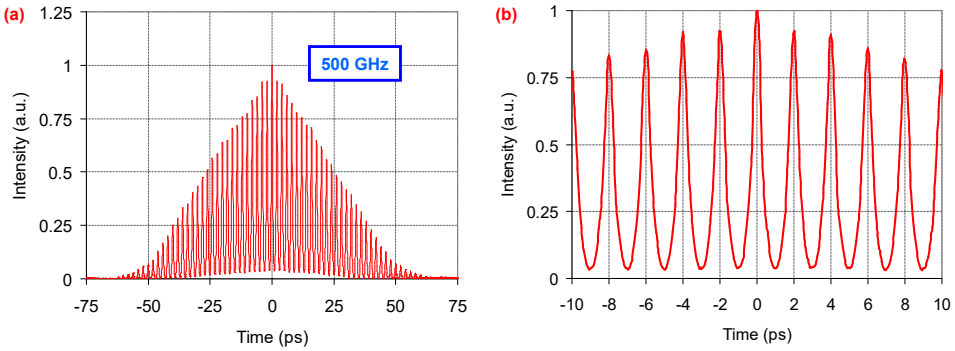

Fig. 9. (a) Autocorrelation of pulse train from the first five stages (32 pulses) of the pulse divider for a set frequency of 500 GHz, (b) Zoomed-in autocorrelation trace showing a pulse separation of 2 ps that is required for resonant excitation at 500 GHz.

The scanning range of the autocorrelator at hand in our experiments was limited to 150 ps, and hence, for the precise setting of the distances in our 6th and 7th stages, we have looked at the variation of THz efficiency around the resonance of the crystal, by scanning each stage separately and looking at the THz yield variation. For example, Fig. 10 shows a frequency scan for the first seven stages independently. As we can see, the THz efficiency is sensitive to the correct adjustment of frequency/delay of stages, and this can be used to optimize the arm lengths. We have used this method to fine-tune all stages' distances to obtain a sharp resonance signal.

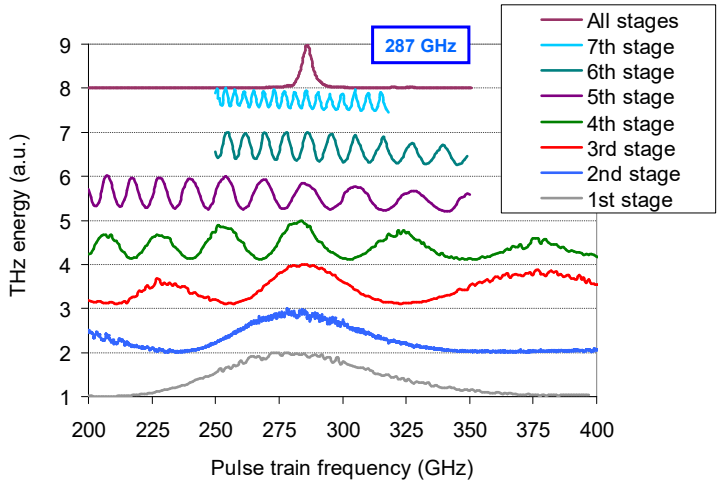

Fig. 10. Optimization of the delay stage arm positions by measuring the effect of stage distance on THz efficiency. Once all the stages are positioned correctly, the pulse train's frequency scan can map the nonlinear crystal's frequency response with high precision.

Once the interferometer distances were adjusted as described above, we tested our system's frequency scan capability. For example, in Fig. 11(a), we show the measured pulse train frequency scan data of the 400 µm QPM period crystal along with other PPLN samples with QPM periods of 330 µm and 600 µm at 78 K and at room temperature. The data is taken using a pulse train with

Optical Materials EXPRESS

128 pulses. We see that a frequency scan with the pulse train source enables a quick but detailed measurement of the frequency response of each crystal [26]. These measurements currently take around ~10 minutes, but we hope to reduce these scanning times to below a minute in future studies once we employ the 1 kHz Yb:YLF laser in our THz system. Hence, this frequency response measurement-based system could be used to quickly identify nonlinear crystals.

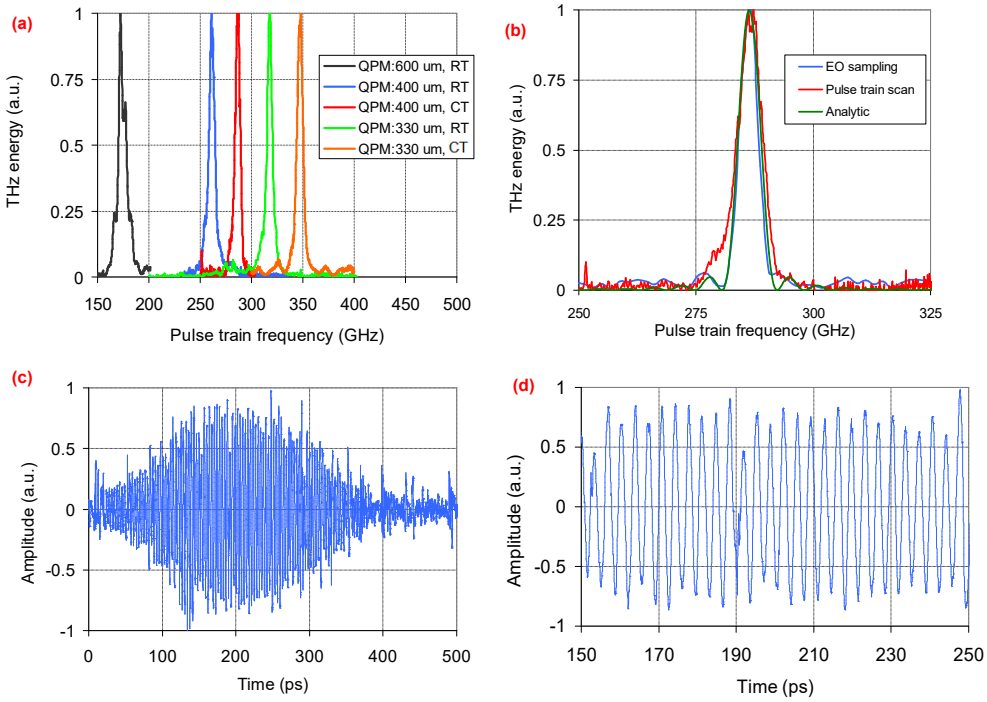

Fig. 11. (a) Frequency response of the PPLN crystals with QPM periods of 600 μm, 400 μm, and 330 μm at cryogenic temperature (CT: 78 K) and room temperatures (RT: ~295 K). The measurement has been performed using the pulse train frequency scan technique. (b) Measured frequency response of the PPLN crystal at 78 K. For comparison, the frequency spectra measured using electro-optic sampling and pulse train frequency scan are shown along with the calculated analytical frequency response curve. (c) Measured electro-optic sampling trace of the long THz pulse generated by the pulse train. The data is collected at 78 K while exciting the crystal with 64 pulses. The THz pulse contains around 100 cycles. (d) The zoomed-in EO-sampling trace between 150 and 250 ps, showing a periodicity of about 3.5 ps.

An alternative method of frequency response measurements is the well-known electro-optic (EO) sampling technique. To independently confirm the calibration of our pulse train frequency scans, we have performed EO sampling with 400 μm QPM period PPLN crystals at 78 K. Figure 11(b) shows the calculated frequency spectrum of the generated THz field from the measured EO sampling data along with the frequency scan approach measurement (details of EO sampling data is shown in Fig. 11(c-d)). As we can see from Fig. 11(b), at 78 K, the PPLN crystal has a peak THz response around 286.5 GHz, and the bandwidth (full width at half maximum, FWHM) of the response curve is around 5 GHz. We can see that within experimental errors, the EO sampling data match the pulse train frequency scan measurement quite well, and both curves are close to the calculated analytical curve (for the analytical curve, we have assumed zero THz absorption).

Optical Materials EXPRESS

Funding. Deutsche Forschungsgemeinschaft (405983224); HORIZON EUROPE European Research Council (609920).

Disclosures. The authors declare no conflicts of interest.

Data Availability. Data underlying the results presented in this paper are not publicly available at this time but may be obtained from the authors upon reasonable request.

References

1. A. Leitenstorfer, A. S. Moskalenko, T. Kampfrath, *et al.*, "The 2023 terahertz science and technology roadmap," J. Phys. D: Appl. Phys. **56**(22), 223001 (2023).
2. J.-H. Son, S. J. Oh, and H. Cheon, "Potential clinical applications of terahertz radiation," J. Appl. Phys. **125**(19), 190901 (2019).
3. A. Herter, A. Shams-Ansari, F. F. Settembrini, *et al.*, "Terahertz waveform synthesis in integrated thin-film lithium niobate platform," Nat. Commun. **14**(1), 11 (2023).
4. K. L. Vodopyanov, "Optical generation of narrow-band terahertz packets in periodically-inverted electro-optic crystals: conversion efficiency and optimal laser pulse format," Opt. Express **14**(6), 2263–2276 (2006).
5. X. Wu, D. Kong, S. Hao, *et al.*, "Generation of 13.9-mJ terahertz radiation from lithium niobate materials," Adv. Mater. **35**(23), 2208947 (2023).
6. T. Kroh, T. Rohwer, D. Zhang, *et al.*, "Parameter sensitivities in tilted-pulse-front based terahertz setups and their implications for high-energy terahertz source design and optimization," Opt. Express **30**(14), 24186–24206 (2022).
7. B. Zhang, Z. Ma, J. Ma, *et al.*, "1.4-mJ high energy terahertz radiation from lithium niobates," Laser Photon. Rev. **15**(3), 2000295 (2021).
8. C. Vicario, B. Monoszlai, C. Lombosi, *et al.*, "Pump pulse width and temperature effects in lithium niobate for efficient THz generation," Opt. Lett. **38**(24), 5373–5376 (2013).
9. F. Giorgianni, B. Wehinger, S. Allenspach, *et al.*, "Ultrafast frustration breaking and magnetophononic driving of singlet excitations in a quantum magnet," Phys. Rev. B **107**(18), 184440 (2023).
10. C. D. W. Mosley, D. S. Lake, D. M. Graham, *et al.*, "Large-area periodically-poled lithium niobate wafer stacks optimized for high-energy narrowband terahertz generation," Opt. Express **31**(3), 4041–4054 (2023).
11. H. T. Olgun, W. Tian, G. Cirmi, *et al.*, "Highly efficient generation of narrowband terahertz radiation driven by a two-spectral-line laser in PPLN," Opt. Lett. **47**(10), 2374–2377 (2022).
12. F. Lemery, T. Vinatier, F. Mayet, *et al.*, "Highly scalable multicycle THz production with a homemade periodically poled macrocrystal," Commun. Phys. **3**(1), 150 (2020).
13. D. Jang and K.-Y. Kim, "Multicycle terahertz pulse generation by optical rectification in $LiNbO_3$, $LiTaO_3$, and BBO crystals," Opt. Express **28**(14), 21220–21235 (2020).
14. S. W. Jolly, N. H. Matlis, F. Ahr, *et al.*, "Spectral phase control of interfering chirped pulses for high-energy narrowband terahertz generation," Nat. Commun. **10**(1), 2591 (2019).
15. F. Ahr, S. W. Jolly, N. H. Matlis, *et al.*, "Narrowband terahertz generation with chirped-and-delayed laser pulses in periodically poled lithium niobate," Opt. Lett. **42**(11), 2118–2121 (2017).
16. S. Carbajo, J. Schulte, X. Wu, *et al.*, "Efficient narrowband terahertz generation in cryogenically cooled periodically poled lithium niobate," Opt. Lett. **40**(24), 5762–5765 (2015).
17. K. Uchida, H. Hirori, T. Aoki, *et al.*, "Time-resolved observation of coherent excitonic nonlinear response with a table-top narrowband THz pulse wave," Appl. Phys. Lett. **107**(22), 221106 (2015).
18. C. Rentschler, N. H. Matlis, U. Demirbas, *et al.*, "Parameter dependencies in multicycle THz generation with tunable high-energy pulse trains in large-aperture crystals," Proc.SPIE **12869**, 44 (2024).
19. O. V Chefonov, A. V Ovchinnikov, C. P. Hauri, *et al.*, "Broadband and narrowband laser-based terahertz source and its application for resonant and non-resonant excitation of antiferromagnetic modes in NiO," Opt. Express **27**(19), 27273–27281 (2019).
20. T. Kubacka, J. A. Johnson, M. C. Hoffmann, *et al.*, "Large-amplitude spin dynamics driven by a THz pulse in resonance with an electromagnon," Science **343**(6177), 1333–1336 (2014).
21. X. Su, D. Wang, Q. Tian, *et al.*, "Widely tunable narrow-band coherent Terahertz radiation from an undulator at THU," J. Instrum. **13**(01), C01020 (2018).
22. Y.-S. Lee, T. Meade, V. Perlin, *et al.*, "Generation of narrow-band terahertz radiation via optical rectification of femtosecond pulses in periodically poled lithium niobate," Appl. Phys. Lett. **76**(18), 2505–2507 (2000).
23. C. Zhang, Y. Avetisyan, G. Abgaryan, *et al.*, "Tunable narrowband terahertz generation in lithium niobate crystals using a binary phase mask," Opt. Lett. **38**(6), 953–955 (2013).
24. A. G. Stepanov, J. Hebling, and J. Kuhl, "Generation, tuning, and shaping of narrow-band, picosecond THz pulses by two-beam excitation," Opt. Express **12**(19), 4650–4658 (2004).
25. J. Ahn, A. V Efimov, R. D. Averitt, *et al.*, "Terahertz waveform synthesis via optical rectification of shaped ultrafast laser pulses," Opt. Express **11**(20), 2486–2496 (2003).
26. N. H. Matlis, Z. Zhang, U. Demirbas, *et al.*, "Precise parameter control of multicycle terahertz generation in PPLN using flexible pump pulse trains," Opt. Express **31**(26), 44424–44443 (2023).
27. A. Buzády, R. Gálos, G. Makkai, *et al.*, "Temperature-dependent terahertz time-domain spectroscopy study of Mg-doped stoichiometric lithium niobate," Opt. Mater. Express **10**(4), 998–1006 (2020).

Optical Materials EXPRESS

28. V. D. Antsygin, A. A. Mamrashev, L. V Maximov, *et al.*, "Temperature dependence of terahertz properties of stoichiometric lithium tantalate," J. Infrared, Millimeter, Terahertz Waves **43**(11-12), 895–904 (2022).
29. K. A. Kuznetsov, G. K. Kitaeva, S. P. Kovalev, *et al.*, "Complex extraordinary dielectric function of Mg-doped lithium niobate crystals at terahertz frequencies," Appl. Phys. B **122**(8), 223 (2016).
30. X. Wu, C. Zhou, W. R. Huang, *et al.*, "Temperature dependent refractive index and absorption coefficient of congruent lithium niobate crystals in the terahertz range," Opt. Express **23**(23), 29729–29737 (2015).
31. A. L. Calendron, H. Cankaya, and F. X. Kartner, "High-energy kHz Yb:KYW dual-crystal regenerative amplifier," Opt. Express **22**(20), 24752–24762 (2014).
32. M. Pergament, M. Kellert, U. Demirbas, *et al.*, "100-mJ, 100-W cryogenically cooled Yb:YLF laser," Opt. Lett. **48**(11), 2833–2836 (2023).
33. U. Demirbas, M. Kellert, J. Thesinga, *et al.*, "Highly efficient cryogenic Yb:YLF regenerative amplifier with 250 W average power," Opt. Lett. **46**(16), 3865–3868 (2021).
34. U. Demirbas, C. Rentschler, Z. Zhang, *et al.*, "Two-dimensional effects in Multicycle THz generation with tunable pump pulse trains in lithium niobate," in *2023 48th International Conference on Infrared, Millimeter, and Terahertz Waves (IRMMW-THz)* (2023), 1–2.
35. T. Kroh, T. Rohwer, L. Wang, *et al.*, "Robust optimization of single-cycle THz setups based on phase-matching via tilted pulse fronts using an incident-fluence metric," Proc. SPIE **11264**(2), 42 (2020).
36. Y. S. Lee, T. Meade, T. B. Norris, *et al.*, "Tunable narrow-band terahertz generation from periodically poled lithium niobate," Appl. Phys. Lett. **78**(23), 3583–3585 (2001).
37. L. Pálfalvi, J. Hebling, J. Kuhl, *et al.*, "Temperature dependence of the absorption and refraction of Mg-doped congruent and stoichiometric LiNbO3 in the THz range," J. Appl. Phys. **97**(12), 123505 (2005).
38. O. Paul, A. Quosig, T. Bauer, *et al.*, "Temperature-dependent Sellmeier equation in the MIR for the extraordinary refractive index of 5% MgO doped congruent $LiNbO_3$," Appl. Phys. B **86**(1), 111–115 (2006).
39. G. J. Edwards and M. Lawrence, "A temperature-dependent dispersion equation for congruently grown lithium niobate," Opt. Quantum Electron. **16**(4), 373–375 (1984).
40. D. H. Jundt, "Temperature-dependent Sellmeier equation for the index of refraction, ne, in congruent lithium niobate," Opt. Lett. **22**(20), 1 (1997).
41. O. Gayer, Z. Sacks, E. galun, *et al.*, "Temperature and wavelength dependent refractive index equations for MgO-doped congruent and stoichiometric $LiNbO_3$," Appl. Phys. B **91**(2), 343–348 (2008).
42. J. S. Browder and S. S. Ballard, "Thermal expansion data for eight optical materials from 60 K to 300 K," Appl. Opt. **16**(12), 3214–3217 (1977).
43. R. Sowade, I. Breunig, C. Tulea, *et al.*, "Nonlinear coefficient and temperature dependence of the refractive index of lithium niobate crystals in the terahertz regime," Appl. Phys. B **99**(1-2), 63–66 (2010).
44. S.-W. Huang, E. Granados, W. R. Huang, *et al.*, "High conversion efficiency, high energy terahertz pulses by optical rectification in cryogenically cooled lithium niobate," Opt. Lett. **38**(5), 796–798 (2013).
45. Y.-S. Lee, T. Meade, M. DeCamp, *et al.*, "Temperature dependence of narrow-band terahertz generation from periodically poled lithium niobate," Appl. Phys. Lett. **77**(9), 1244–1246 (2000).
46. Y. Liu, G. Ren, T. Cao, *et al.*, "Modeling temperature, frequency, and strain effects on the linear electro-optic coefficients of ferroelectric oxides," J. Appl. Phys. **131**(16), 163101 (2022).
47. C. Herzog, G. Poberaj, and P. Günter, "Electro-optic behavior of lithium niobate at cryogenic temperatures," Opt. Commun. **281**(4), 793–796 (2008).
48. P. Górski, R. Ledzion, K. Bondarczuk, *et al.*, "Temperature dependence of linear electrooptic coefficients r113 and r333 in lithium niobate," Opto-Electronics Rev. **16**(1), 46–48 (2008).